Specific heat dependence on orientational order at cylindrically confined liquid crystal phase transitions

Germano S. Iannacchione and Daniele Finotello
Department of Physics and the Liquid Crystal Institute, Kent State University, Kent, Ohio 44242
(Received 8 February 1994)

Results from a high resolution calorimetric study for the alkylcyanobiphenyl liquid crystal series *n*CB, with *n* the number of carbons in the alkyl chain, confined to the 0.2 μm diam cylindrical pores of Anopore membranes are reported. The orientational order at the pore wall is controlled and varied from tangential to homeotropic by surface treatment. Effects due to confinement and director configuration on the specific heat were studied at the weakly first-order nematic to isotropic, the continuous smectic-*A* to nematic, and the first-order smectic-*A* to isotropic phase transitions. Deviations from bulk are considerable and the confined specific heat, strongly dependent on the orientational order, is dominated by elastic distortions and influenced by surface order and disorder contributions. A surface induced nematiclike ordered shell near the pore wall is retained deep in the isotropic phase. Over a limited reduced temperature range bulklike criticality appears to be preserved under confinement. The average scalar orientational order parameter temperature dependence can be extracted from the specific heat results using a simplified Landau–de Gennes theory and is found to be consistent with nuclear magnetic resonance measurements. In spite of the large pore size, the smectic translational order within the pores is inhibited for liquid crystals that also exhibit a nematic phase.

PACS number(s): 64.70.Md, 61.30.−v, 65.20.+w, 82.60.Fa

I. INTRODUCTION

Studies of phenomena for physical systems in geometries more restrictive than bulk are receiving considerable attention. Cylindrically confined liquid crystals studies include effects on the orientational and translational order and phase transitions under controlled conditions. Surface phenomena are enhanced by modifying the surface with surfactants and/or by varying the size of the confining length. Because the weak orientational and translational order are influenced by the presence of surfaces, the existence of long range correlations near a phase transition, and the presence of different order phase transitions, liquid crystals are a unique system to test in restricted geometries. Effects due to substrate disorder on local properties such as the director configuration within the pores or on global thermodynamic properties such as the specific heat can be addressed. In general, studies of the influence of disorder on physical properties are a topic of current interest [1–4].

Deuterium nuclear magnetic resonance (^{2}H NMR) is highly sensitive to the orientational order and director configurations within submicrometer size cavities. Several phenomena were discovered through ^{2}H NMR studies as a function of pore size for 5CB confined to polycarbonate Nuclepore membranes [5] and as a function of pore surface treatment using aluminum oxide Anopore membranes [6]. In Nuclepore, at temperatures in the isotropic phase clear evidence of a weak orientationally ordered molecular layer at the pore wall and a temperature independent surface order parameter were found. Results in the nematic phase lead to the experimental determination of the K_{24} elastic constant [7]. In Anopore, the degree of orientational order at the pore surface and the surface coupling constant were determined for a variety of pore surface treatments [6].

In this work we describe specific heat measurements on the alkylcyanobiphenyl (*n*CB) series ($n=5,7,8$, and 10) confined to the 0.2 μm diam, 60 μm long cylindrical pores of Anospore membranes. These studies probed the weakly first-order nematic to isotropic (N-I), the continuous smectic-*A* to nematic (Sm*A*–*N*), and the first-order smectic-*A* to isotropic (Sm-*A*–*I*) phase transitions using untreated Anopore membranes and after pore surface treatment with egg-yolk lecithin. A shorter version of this study was recently published [8].

The highlights of these results are that the specific heat is strongly dependent on the liquid crystal configuration within the pore. Specific heat peaks at depressed transition temperatures are rounded, broadened, and suppressed as compared to bulk. The pore surface has the dual role of inducing orientational order near the pore wall while disordering effects exist far from them. Smectic ordering is inhibited for liquid crystals with a nematic phase; surprisingly, such translational order does not appear to be strongly affected if the nematic phase is absent in the parent bulk liquid crystal. Using a simplified Landau–de Gennes model, successfully employed for 5CB confined to Vycor glass [9], the average scalar order parameter temperature dependence near the *N*-*I* transition is extracted from the measured specific heat and is found to be in agreement with the ^{2}H NMR results [10].

This paper is organized as follows. We first describe the experimental technique and apparatus, the properties of the Anopore substrate, and the samples preparation. In Sec. III we discuss the specific heat results and data

analysis according to the order of the phase transition. Finally, we summarize the most important results and suggest alternative studies.

II. EXPERIMENTAL TECHNIQUE

We have used an ac calorimetric technique on low temperature studies of the localized and superfluid properties of helium films absorbed in Anopore membranes [11] and for the present liquid crystal study. Although we have detailed the implementation of the technique at these different temperature regimes recently [12], we highlight below those aspects more relevant to this work.

A. ac calorimetry and experimental apparatus

In the ac calorimetry technique [13], measurements are performed under nearly equilibrium conditions: the sample is set into small temperature oscillations about an average temperature allowing the implementation of signal averaging routines, lock-in amplification, and total computer automation. A relative heat capacity resolution of at least 0.2% is achieved often using a small amount of material. Strict thermal isolation of the sample from its surroundings is not required; thus ac calorimetry is adaptable for studies of physical systems over many temperature ranges. Examples of its low temperature applications include studies of helium films adsorbed in porous glasses [14] and those of superconducting films [15]. At or above room temperature examples include the study of bulk liquid crystal phase transitions [16] and high resolution studies of free-standing liquid crystal films only a few molecules thick [17]. Because of its oscillatory nature, ac calorimetry is not the ideal technique to probe strongly first-order transitions.

In the ac technique, heat is applied sinusoidally to a sample; the amplitude of the resulting temperature oscillations is inversely proportional to the sample's heat capacity. When the oscillating voltage is applied to a resistive wire heater, Joule's heat is generated at a rate $Q=Q_0\cos^2(\omega_v t)=\frac{1}{2}Q_0[1+\cos(2\omega_v t)]$, where $\omega_v=2\pi f_v$ is the angular voltage frequency and Q_0 is its heating amplitude. The induced temperature oscillations are at twice the voltage frequency $\omega=2\omega_v$.

The thermal model consists of a heater of heat capacity C_h and thermal conductance K_h, a thermometer with C_θ and K_θ, and a sample with C_S and K_s linked to a cell. The cell, of low heat capacity C_C and good thermal conductivity, is the structure that supports or contains the sample. The complete arrangement of total heat capacity $C=C_h+C_\theta+C_s+C_C$ is linked through a conductance K_b to a thermal bath regulated at T_b. The heat balance equations are written in terms of the heat capacities and thermal conductivities of the sample, heater, and thermometer, and the applied power [13]. The temperature at the cell thermometer is given by

$$T_\theta=T_b+\frac{Q_0}{2K_b}+\frac{Q_0}{2\omega C}\left[1+\frac{1}{(\omega\tau_e)^2}+\omega^2(\tau_\theta^2+\tau_h^2+\tau_s^2)\right]^{1/2}\times\cos(\omega t-\alpha)\ . \quad (1)$$

The second term $T_{\rm dc}=Q_0/2K_b$ is the rise in sample temperature above T_b from the rms heating, while the last term is the induced temperature oscillation of amplitude $T_{\rm ac}$, also expressed as

$$T_{\rm ac}=\frac{Q_0}{2\omega C}\left[1+\frac{1}{(\omega\tau_e)^2}+\omega^2\tau_i^2\right]^{1/2}, \quad (2)$$

where $\tau_e=C/K_b$ and $\tau_i^2=(\tau_\theta^2+\tau_h^2+\tau_s^2)$ are the external and internal thermal relaxation times, respectively, τ_i is the time required for the system to reach equilibrium with the applied heat, and τ_e is the time required from equilibrium with the thermal bath. The internal relaxation times are defined as $\tau_\theta=C_\theta/K_\theta$, $\tau_h=C_h/K_h$, and $\tau_s=C_S/K_S$. The cell's internal time constant is usually negligible.

Frequency plays an important role in an ac technique. If the inverse of the applied heating frequency is "slower" than the internal time τ, but "faster" than the external time τ_e (hence losing a negligible amount of heat to the bath), then

$$\frac{1}{\tau_e}<\omega<\frac{1}{\tau_i}\ . \quad (3)$$

Once these conditions are satisfied, the term in large parentheses in Eq. (2) is of order unity and

$$C\cong\frac{Q_0}{2\omega T_{\rm ac}}\ . \quad (4)$$

In terms of experimentally measurable quantities, the heat capacity becomes [12]

$$C=\frac{V_{pp}^2T^2IR_{\rm th}}{32\sqrt{2}f_vR_h}[A_1+2A_2\ln(R_{\rm th})+3A_3\ln(R_{\rm th})^2+\cdots]^{-1}, \quad (5)$$

where V_{pp} is the applied peak-to-peak voltage, T is the average sample temperature, R_h is the heater resistance, $R_{\rm th}$ is the thermometer resistance, I is the dc current biasing the resistive thermometer, and the coefficients A_i arise from the temperature calibration of the thermometer.

The external time constant (the thermal link to the regulated bath) is achieved through the heater and thermometer electrical leads. Typically 30–60 s, it is adjusted by selecting the appropriate material, length, and cross-sectional area for the leads. The internal time constant arises from the heat capacity and thermal conductivity of the sample so it depends on its thickness; the time constants from the thermometer and heater are typically short and usually temperature independent. To satisfy Eq. (3), the sample thickness must be less than the thermal diffusion length $l=(2K_SA/\omega C_S)^{-1/2}$, where A is the cross-sectional area of the sample. If the thickness is larger than l, then the sample will not reach equilibrium with, nor will it follow, the imposed oscillations.

Equation (3) is tested by a frequency scan. This is done by maintaining all parameters (bath temperature and applied power) constant, while varying the frequency of the applied heat and measuring the temperature response.

There are two equivalent ways of representing such a frequency scan and determining the proper operating frequency. The first is to construct a log-log plot of $2f_v T_{ac}$ versus $2f_v$, which will show a frequency "plateau" that indicates the frequency regime where neither τ_e nor τ_i contributes significantly to T_{ac}. Equivalently, plotting T_{ac} versus $(2f_v)^{-1}$ will show a region where a straight line through the origin may be drawn; see Eq. (2). Within this linear region (or the plateau), Eq. (3) is satisfied and the specific heat is frequency independent. Both types of plots are illustrated in Fig. 1 for an empty cell and for the same cell with a confined liquid crystal sample present. The addition of the sample is reflected in the high frequency roll-off now occurring at lower frequencies.

The induced temperature oscillations will be out of phase with respect to the applied heat. From Eqs. (1) and (2), there is a phase shift α given by [12]

$$\tan(\alpha)=\left[\frac{1}{\omega\tau_e}-\omega\tau_i\right]^{-1}. \tag{6}$$

Evidently the phase shift contains information on the heat capacity and thermal conductance of the sample mixed with thermal contributions from the addendum materials. It has been empirically observed (see also Ref. [16]) that there is a typical phase shift signature depending on the order of the phase transition. At a weakly first-order transition, there exists a narrow peak which is interpreted as a region of two-phase coexistence and brackets the temperature at which the latent heat is released. Presumably, the sample cannot easily follow the imposed oscillations, resulting in an increase of the phase shift [16]. At a continuous transition, there is often a decrease in α likely due to the lack of a latent heat and a correlation length which grows to macroscopic scales; in some cases, it may not be experimentally detectable. Finally, at a first-order transition, the phase shift signature mimics that of the specific heat, very likely reflecting a two-phase region. Figure 2 illustrates typical phase shifts at the N–I, Sm-A–N, and Sm-A–I transitions as well as the heat capacity for bulk 8CB and 10CB. What is significant are changes in the phase shift in the vicinity of a transition with respect to a "regular," mildly temperature dependent background also shown in Fig. 2.

A block diagram for the electronics is shown in Fig. 3. The signal generator references the lock-in amplifier (LIA) and heats the cell through its heater. The bath is

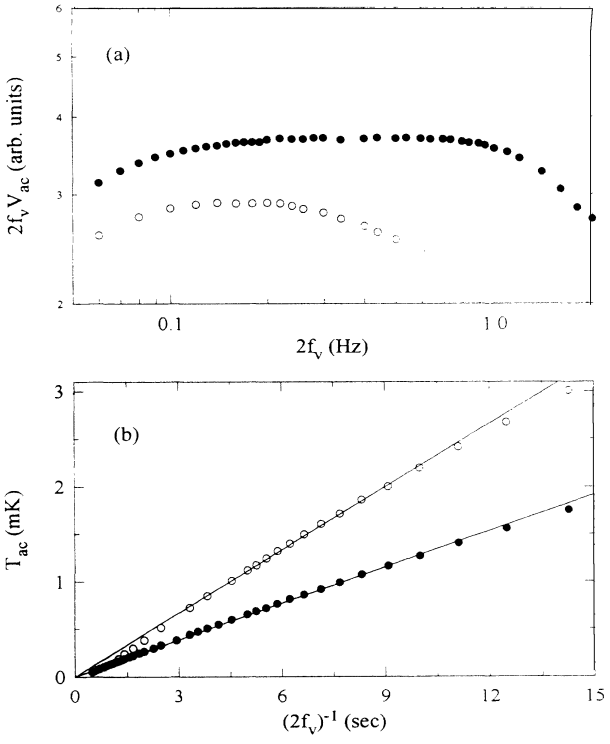

FIG. 1. Equivalent plots for typical frequency scans for the empty calorimeter (●) and with a confined liquid crystal sample present (○). (a) The plateau area and (b) the linear region indicate the specific heat frequency independent regime. The primary effect of the sample is to lengthen the internal time constant. In (b) the cell + sample frequency scan used 1.85 times more power and at a higher temperature than in (a) on the same sample, hence the higher T_{ac} as compared to the empty cell.

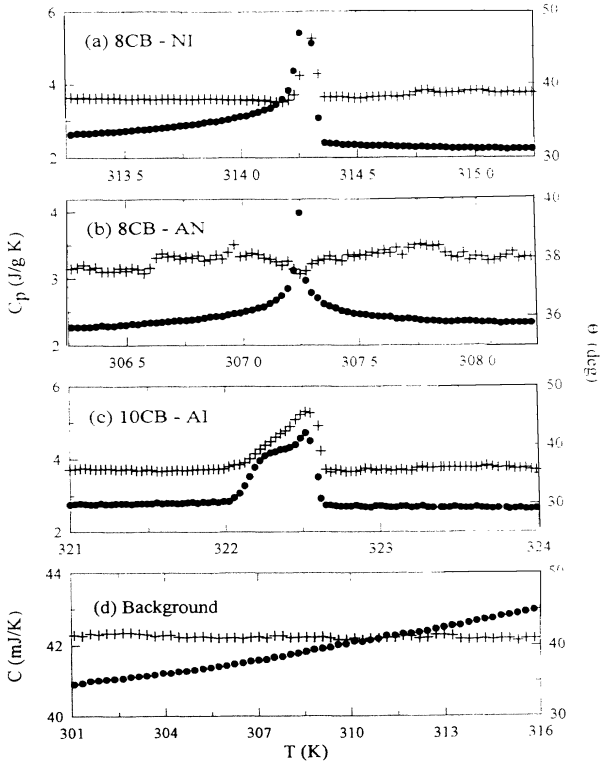

FIG. 2. Phase shift (+) and specific heat (●) for bulk liquid crystals showing the typical signatures at (a) the weakly first-order N-I transition of 8CB, (b) the continuous Sm-A–N of 8CB, and (c) the first-order Sm-A–I of 10CB phase transition. The bottom panel shows the featureless empty cell behavior.

regulated using a resistance bridge/temperature controller system. The magnitude of the induced thermal oscillations and the average sample temperature are detected with the dc biased (at most 73 μA) cell thermometer. The induced oscillations are filtered and amplified and then fed to a low frequency two-phase lock-in amplifier operating in $2f$ mode. The heat capacity (in-phase output of the LIA) as a function of temperature is acquired by maintaining constant power into the cell while changing the temperature of the bath; the phase shift is obtained from the LIA out-of-phase output.

Schematic diagrams for the calorimeter and experimental cell are shown in Fig. 4. A solid brass cylinder is machined to form a concentric cylindrical cavity with one open end creating a "ring." The open end is eventually sealed with a brass cap. The temperature of this ring is the regulated "bath" temperature. Penetrating from the closed end are the electrical connections for the cell thermometer and heater. A cavity is drilled in the ring wall, parallel to the cylinder axis, to snugly accommodate a calibrated 100 Ω platinum thermometer. Wrapped around the exterior of the ring is a manganin resistive heater wire, 0.13 mm cross section. The brass ring is supported by a 3 mm diam, 40 mm long brass post providing the thermal link to a larger, evacuated copper chamber that rests on a large aluminum block partly submerged in a water bath. Foam is used inside the ring to occupy most of its open volume. With this arrangement, data in the temperature range between 290 and 400 K with a control better than 100 μ K are obtained.

The calorimeter cell consists of a 10 kΩ carbon flake thermobead and a 47.7 Ω Evanohm wire (28 Ω/cm, 0.0038 cm cross section) heater attached to the same side of a 10 mm diam, 0.1 mm thick sapphire disk. Sapphire was chosen for its rigidity, flatness, high thermal conductivity, and low heat capacity. The resistive thermobead, a glass encapsulated carbon flake, has the advantage of its extremely small size, ≤ 0.05 mm on side, with a short internal time constant. Small amounts of GE varnish are used to attach the thermobead and heater to the sapphire disk. The temperature sensor, heater, and sapphire disk arrangement have an internal time constant of ~ 1.26 s (a $f_v = 0.79$ Hz, high frequency roll-off).

The heater and thermistor leads are thermally anchored to the brass ring. Coiled copper leads, 80–100 mm long and 0.22 mm in diameter, producing an external time constant of ~ 31.4 s corresponding to a $f_v = 0.032$ Hz, low frequency roll-off, were used. The addendum (empty cell) heat capacity, which was first measured and then subtracted from all data shown below, is nearly

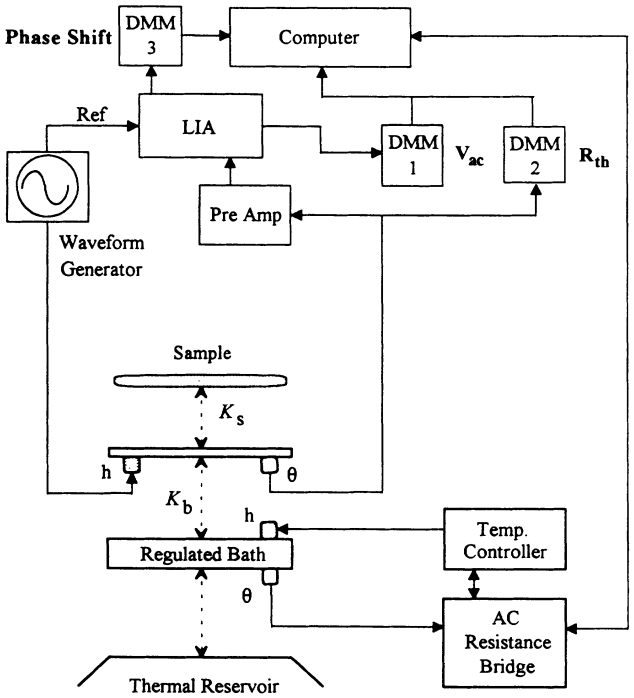

FIG. 3. Schematic diagram illustrating the electronic configuration employed to simultaneously measure the heat capacity and the phase shift. The lock-in amplifier (LIA) operates in $2f$ mode. DMM1 and DMM3 are $5\frac{1}{2}$ digits digital multimeters; DMM2 is a $7\frac{1}{2}$ digit multimeter operating in resistance mode to dc bias the cell thermometer. θ represents thermometers, while h represents resistive wire heaters.

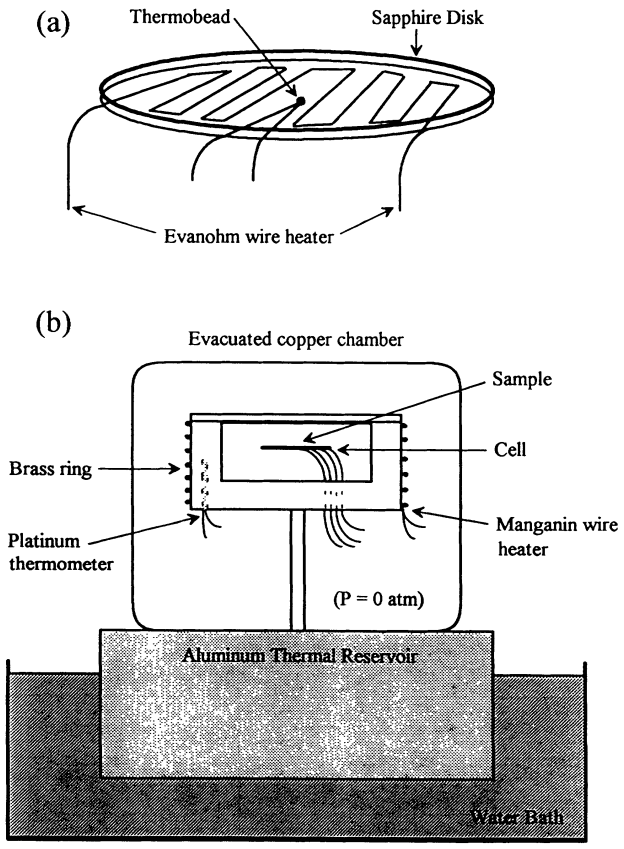

FIG. 4. Illustration of (a) the calorimeter cell and (b) the experimental support apparatus.

linear changing from 42 mJ/K at 303 K to 46 mJ/K at 317 K. From frequency scans at several temperatures, the voltage frequency was typically 0.055 Hz; the induced oscillations were usually 2 mK peak to peak. Data were taken in 5–10 mK temperature steps; after waiting 7 min to reach equilibrium at the new temperature, the data were averaged for 8 min ($\sim$1000 points) at each temperature. The relative heat capacity resolution is $\sim$0.15% or 75 μJ/K.

B. Substrate properties and confined sample preparation

Anopore membranes [18] are made from an inorganic aluminum-oxides matrix using an electrochemical anodizing process [19]. The anodizing voltage controls the pore size and density. The pores that form are cylindrical and extend parallel to one another through its 60 μm thickness Anopore have a sharply centered pore size distribution, with over 90% of the pores at the rated 0.2 μm diameter. From nitrogen adsorption isotherms and scanning electron microscopy (SEM) [20], their porosity is nearly 40%. The SEM photograph in Fig. 5 illustrates these characteristics.

Anopore were cut to $\leq$10 mm diam disks. These disks were cleaned in an acetone or ethyl alcohol ultrasonic bath and dried in an oven. For the lecithin pore treatment, chosen because of the existing NMR data, the disks were immersed in a 2% solution of egg-yolk lecithin and hexane or chloroform. Although the treated disks appear to dry quickly when removed from the surfactant bath, they were placed in a vacuum oven at 70 °C for total solvent removal. Treated or untreated, all disks were immersed in an isotropic bath of the desired *n*CB liquid crystal; they were turned and rearranged within the bath several times for 3 h. The excess material on the outer surfaces of the disks was removed by squeezing them between Whatman filtration paper.

For all measurements, a *single* filled Anopore disk, total mass 6–7 mg containing 2–2.5 mg of liquid crystal, was placed on the cell and cycled through the bulk isotropic transition several times. This annealing process was performed to ensure that the director field had reached its final stable configuration. Good thermal contact was achieved thanks to the flatness of both sapphire and Anopore; both surfaces do not deviate by more than 1 μm over the contact area. After individual addendum subtraction, similar heat capacities (to within 5%, even less near a transition) were measured whether or not the membrane was tied with dental floss or simply rested onto the cell. Results also reproduced when the samples were sandwiched by a second sapphire disk provided with a thermometer to detect the thermal oscillations.

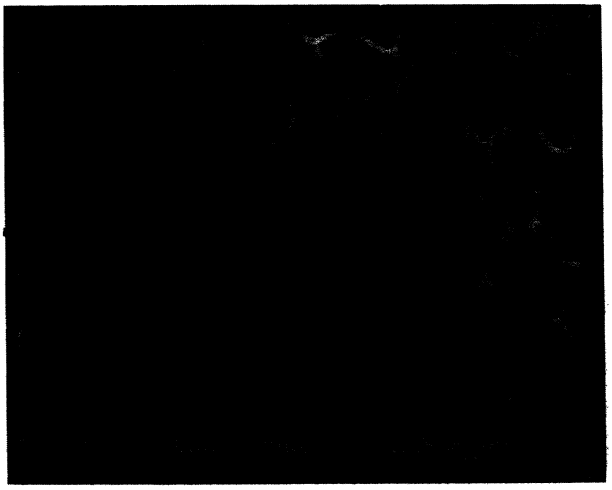

FIG. 5. SEM photograph of the 0.2 μm diam pores of Anopore membrane.

III. RESULTS AND DISCUSSION

For untreated Anopore, the director is aligned tangential to the pore cylindrical axis, or axially aligned. After the lecithin treatment, the alignment is homeotropic (radial) to the inner pore surface [6]. In general, for a cylindrical geometry there exist several possible radial configurations [21]; here the nematic director configuration is most likely an escaped radial with point defects; the director starts perpendicular at the pore wall and then gradually bends parallel to the pore axis near its center. For the radial configuration, both the order parameter and the director field have spatial dependence, while in the axial configuration, there exists a spatially dependent order parameter with a uniform director field parallel to the pore axis. As shown below, the confined specific heat is strongly dependent on the director configuration.

A. Nematic to isotropic transition

Specific heat results near the *N-I* transition for bulk, axial, and radial confined samples of 5CB, 7CB, and 8CB are presented in Figs. 6–8. Several features are evident. The magnitude of the bulk specific heat in the isotropic phase and the transition temperature are consistent with those in the literature. For all liquid crystals and both alignments, a suppressed, rounded, and downward shifted in temperature specific heat peak is found; differences in the magnitude of the specific heat from bulk far from the transition are negligible. Comparing between the confined cases, transition temperature shifts, peak height suppressions, and broadening of the *N-I* transition are enhanced for the radial case. With respect to bulk, the transition temperature for the axial case is shifted down by 0.44, 0.87, and 0.75 K for 5CB, 7CB, and 8CB, respectively. In the radial case, nearly three times larger shifts of 1.15, 2.36, and 1.41 K for 5CB, 7CB, and 8CB, respectively, are found. These shifts are comparable to other confined systems [22,23] and reproduced to better than 0.1 K when repeated with membranes from different branches. Table I summarizes these results.

The transition width, as determined by the full width at half maximum (FWHM) of the specific heat peaks, broadens from the axial to radial alignment. In the former, the specific heat peak retains the sharp, bulklike decrease on the isotropic side of the transition, while in the

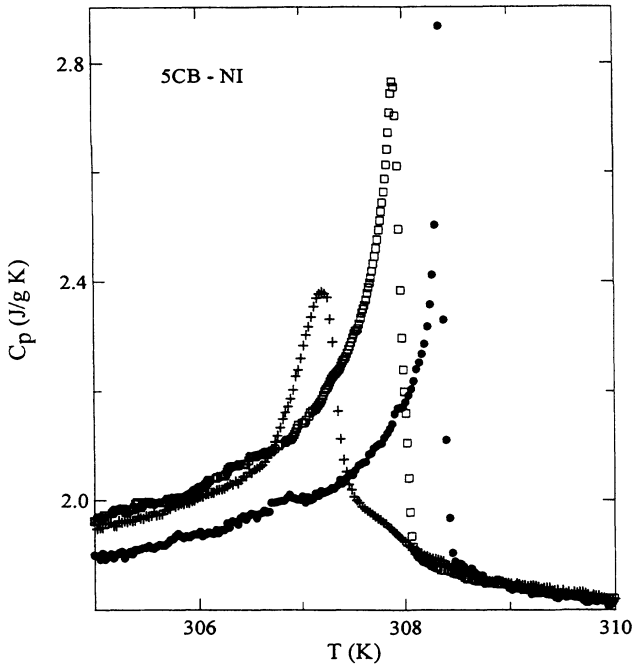

FIG. 6. Specific heat as a function of temperature near the *N-I* transition for bulk (●), axial (□), and radial (+) 5CB configurations.

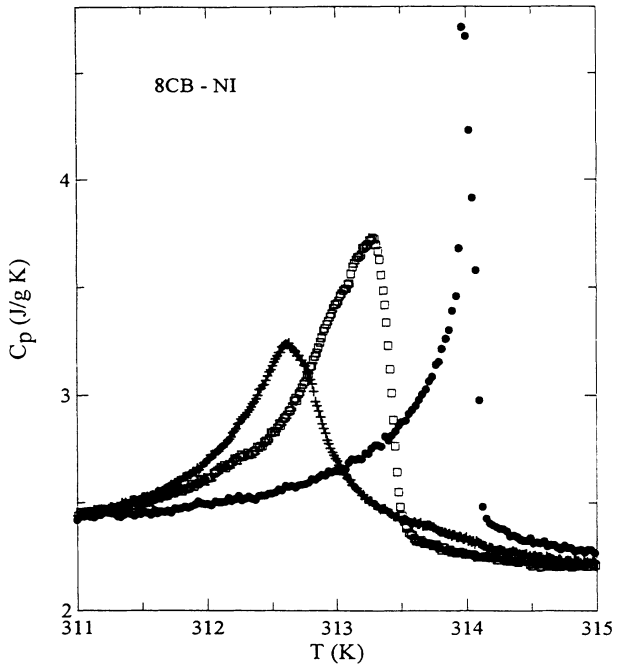

FIG. 8. Specific heat as a function of temperature near the *N-I* transition for bulk (●), axial (□), and radial (+) 8CB configurations.

latter, the peak appears rather symmetric about the transition temperature T_C ($T_C = T_{NI}$ for bulk).

For all samples at the same reduced temperature $t = |T/T_C - 1|$, near and *above* T_C, the magnitude of the specific heat is higher for the radial case than for the axial or the bulk case. This is due to residual surface induced nematic order near the pore wall [5,6]. The specific heat for the axial case is slightly above that for the bulk case, indicating that the thermal fluctuations for this system are similar to those of the bulk case. The residual nematic order at the untreated pore wall is small and temperature independent, while for the lecithin treated pores it is large, decreasing with increasing temperature [6].

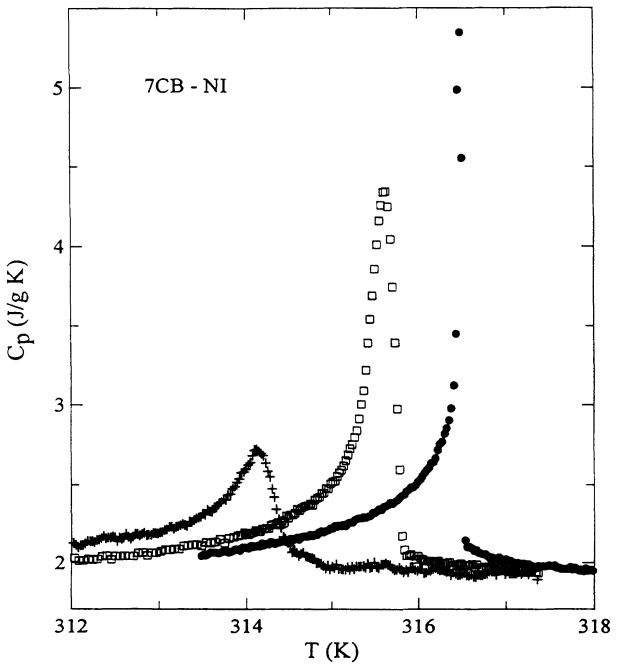

FIG. 7. Specific heat as a function of temperature near the *N-I* transition for bulk (●), axial (□), and radial (+) 7CB configurations.

For all samples at the same t near and *below* T_C, the behavior is different. The bulk specific heat magnitude is intermediate between the lower axial and the higher radial values. This may be understood by considering the spatial dependence of both the order parameter and the director. For the radial case, the thermal fluctuations of the order parameter may be suppressed by the additional spatial dependence of the director, leading to the lowest nematic specific heat magnitude. For the axial case, the director is uniform across the pore, but the degree of order near the pore wall is less than that near the pore center. This would increase order fluctuations between nematic domains near the pore center and those near the wall, consequently producing a higher than bulk specific heat. The jump in the specific heat at T_C ($=T_{NI}$), obtained from extrapolating the nematic and isotropic phases far from the transition to T_C [24], appears to be unaffected by confinement.

The effects of surface anchoring must be incorporated to understand the suppression of the specific heat peak maximum at T_C. As the temperature increases across the transition, only the liquid crystal near the pore center disorders, the rest remaining ordered (pinned) by the surface deep in the isotropic phase. There is no clear boundary between these two regions and the order changes gradual-

TABLE I. Thermodynamic characteristics of the N-I transition for bulk, axial, and radial 5CB, 7CB, and 8CB. ΔT is the shift from the bulk T_{NI}, ΔC_p the specific heat maximum at T_{NI} above the background, ΔC_{NI} the difference in specific heat between the nematic and isotropic phase at the same temperature distance from T_{NI}, and ΔH the area under the specific heat curve (enthalpy) over the same temperature range about T_{NI}. FWHM is the full width at half maximum.

nCB	System	T_{NI} (K)	ΔT (K)	ΔC_p (J/g K)	ΔC_{NI} (J/g K)	FWHM (K)	ΔH (J/g)
5CB	bulk	308.33		1.07	0.12	0.32	1.16
	axial	307.89	−0.44	0.95	0.14	0.51	1.17
	radial	307.18	−1.15	0.56	0.12	0.68	0.99
7CB	bulk	316.48		3.41	0.17	0.09	1.33
	axial	315.61	−0.87	2.41	0.16	0.37	1.76
	radial	314.12	−2.36	0.78	0.16	0.79	1.07
8CB	bulk	314.02		2.51	0.23	0.16	2.13
	axial	313.27	−0.75	1.52	0.26	0.78	2.07
	radial	312.62	−1.4	1.03	0.16	0.96	1.76

ly across the pore diameter. Surface pinning prevents the liquid crystal from undergoing the transition at T_C (equivalent to surface immobilization); higher temperatures are required to slowly free them, thus rounding and broadening the transition. As the surface pinning increases from the axial to the radial case, less material undergoes the transition in the latter and the specific heat, calculated by dividing the heat capacity by the total liquid crystal mass, is smaller. The surface coupling constant, which is a measure of the surface anchoring strength, is an order of magnitude larger for the lecithin treated than for the untreated Anopore [6].

To illustrate this pinning phenomenon, for the axial 5CB, the specific heat peak is suppressed by 12%, but overall resembles the bulk one. If 12% of the molecules were pinned, it would correspond to a surface induced nematic cylindrical shell ~62 Å thick. Such nematic pinning lengths are not unreasonable in light of dielectric spectroscopy and diffusion studies also interpreted in terms of similar thickness surface induced nematic (polar ordered) shells [25,26]. Supporting evidence for a pinning model can be extracted from the transition enthalpy ΔH, calculated from the area under the specific heat curve over a similar temperature range enclosing T_C. The enthalpy for the radial 5CB, where the peak is a factor of 2 broader than that of the bulk case and clearly rounded, is smaller than that of the bulk case by ~17%, corresponding to an ~78 Å surface induced nematic pinning length.

Downward T_C shifts, introduced by surface disordering effects and simultaneous specific heat peak suppressions, understood in terms of a pinning model, could be attributed to impurities. If this were the case, and since the purity of all liquid crystals was determined by chromatography to be better than 99.9%, any impurities would be intrinsic to the membranes, with a larger amount present in the treated pores. As previously mentioned, similar T_C shifts (to within 0.1 K, an order of magnitude less than the shifts from bulk) and peak suppressions (to a few percent) were found when using membranes from different batches. Yet, to investigate the effect of impurities introduced by the possible detachment of lecithin from the pore wall, specific heat measurements for mixtures of 5CB and lecithin were performed. It was found that even for nearly 50% of lecithin added to bulk 5CB, the effects were small. As seen from Fig. 9, the data for the mixtures and that of the bulk

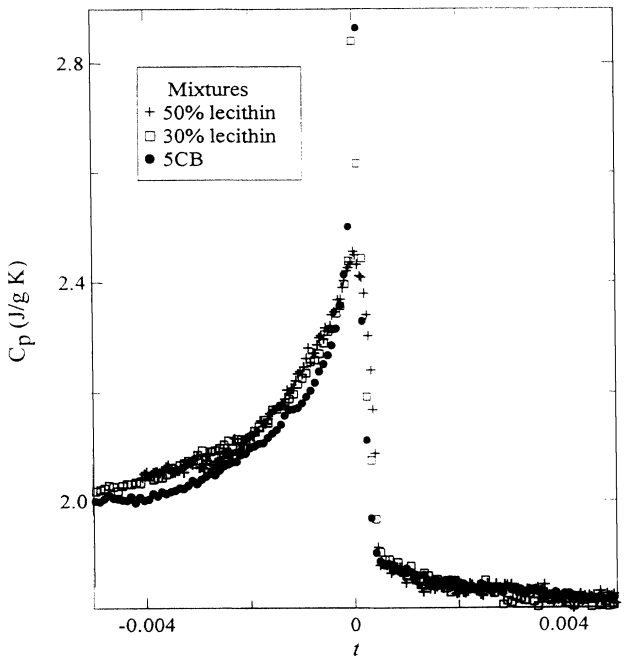

FIG. 9. Specific heat against reduced temperature near the N-I transition of 5CB for bulk and two mixtures of 5CB and lecithin. Concentrations are best estimates. Notice the similar pretransitional effects. The transition temperatures are 308.327, 308.308, and 308.104 K for bulk, 30% and 50% mixtures, respectively.

overlap quite nicely, showing similar pretransitional effects. Extrapolating from this study, the largest possible contamination in the radial case (3–5 % if *all* lecithin detached from the pore wall) would introduce a shift of ~0.01 K and at most a 5% peak reduction. These effects are far too small to account for our results.

Since the correlation length at T_{NI} (~170 Å) is much shorter than the Anopore 1000 Å radius, transition shifts cannot be attributed to finite size effects. Alternatively, due to the rigid pore walls, another cause for transition shifts are surface tension effects introduced via the density difference between the nematic and the isotropic phase. At constant volume, an interface within the pore must form to accommodate the density change at T_C. The effect on the transition temperature may be calculated from [27,23]

$$\Delta T = \frac{2\Delta\sigma T_{NI}}{R\,\Delta H n} \tag{7}$$

where $\Delta\sigma$ is the difference in surface tension between the nematic and isotropic phase, ΔH is the enthalpy of the N-I transition, n is the number density of the liquid crystal, and R is the confining size. Using typical values for bulk 5CB [21,23] ($\Delta\sigma \cong 0.26\times10^{-3}$ N/m, $\Delta H \cong 2.085\times10^{-21}$ N m/$\mathcal{N}$, $n \cong 0.5\times10^{28}$ $\mathcal{N}$/m^3, and $T_{NI} \cong 308$ K, where $\mathcal{N}$ is the number of molecules) and $R = 1000$ Å, a downward shift of 0.16 K would be introduced, compared to the ~1 K typical T_C shift.

Downward temperature shifts may arise from elastic deformation of the nematic director, which are expected to influence these results, and particularly those for the radial configuration. An estimate for such a shift can be obtained from [23]

$$\Delta T = \frac{K_0}{2a_0}\left[\frac{2\pi}{R}\right]^2 . \tag{8}$$

Using 5CB values for the Frank elastic constant $K_0 \approx 5.5\times10^{-11}$ N and the Landau–de Gennes free energy expansion constant $a_0 = 2a/3 = 9.0\times10^4$ J/m^{3}K (see Ref. [23] and Sec. III B below), the downward shift is $\Delta T \cong 1.2$ K, in good agreement with the measured shifts. This estimate assumes a temperature shift in an infinite system with an imposed deformation of wavelength R, which is closely realized in Anopore due to the very narrow distribution of pore sizes. Similar arguments invoking simple elastic distortions were used for 8CB confined to the 3D multiply connected 200 Å diam Aerogel pores to account for the transition shift [22]. Although Aerogel has a wide distribution of pore sizes, a well defined mean pore size exists, allowing the use of a simple elastic distortion model.

Simultaneous phase shift measurements for bulk, axial, and radial 7CB are shown in Fig. 10. For the bulk, the typical sharp peak associated with the fluctuations of the two-phase coexistence region, a hallmark of a weakly first-order transition, is found. For the axial case, the phase shift shows a broad and rounded peak extending over the same temperature width of the rounded portion of the specific heat peak. The coexistence region is greatly broadened by the confinement possibly due to the presence of nematic domains with different degrees of order. The phase shift for the radial case is remarkably different. Instead of a peak, a pronounced dip at a temperature above that of the specific heat maximum is evident. Although a decrease in the phase shift is a signature of a continuous transition (see the Sm-A–N transition in Fig. 2), because of the strong influence of elastic distortions, such a dip could be related to changes in the thermal diffusivity within the pores.

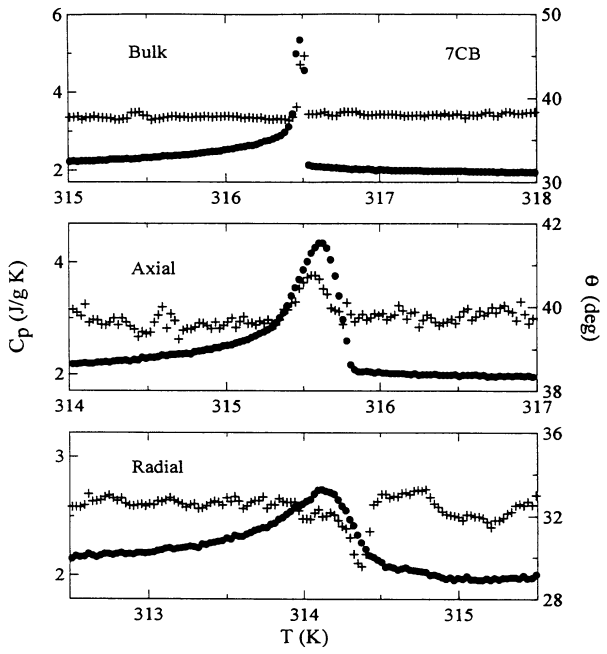

FIG. 10. Phase shift (+) and specific heat (●) near the N-I transition of 7CB for bulk, axial, and radial configurations to emphasize the change in the nature of the phase shift signature, which for the radial configuration resembles that at the 8CB Sm-A–N transition shown in Fig. 2.

The bulk critical behavior can be extracted by fitting the specific heat signature at the N-I transition to a power-law model with a critical exponent α, which determines the universality class of the transition. Due to its weakly first-order nature, the specific heat should diverge to different temperatures when above or below the N-I transition. The power-law exponent should be the same on both sides of the transition. A standard accepted expression is [28–30]

$$C_p = B + D\left[\frac{T}{T_\pm}-1\right] + A_\pm\left|\frac{T}{T_\pm}-1\right|^{-\alpha}, \tag{9}$$

where $\pm$ denotes above and below the transition, respectively. T_+ is the temperature which the isotropic behavior diverges to (T^*) and T_- is the temperature towards which the nematic behavior diverges (T^{**}); $T_- > T_+$ always. The constant and linear terms are identical at both sides of the transition forming the "regular" background. The last term is the critical power-law divergence; for mean field Landau–de Gennes and tricrit-

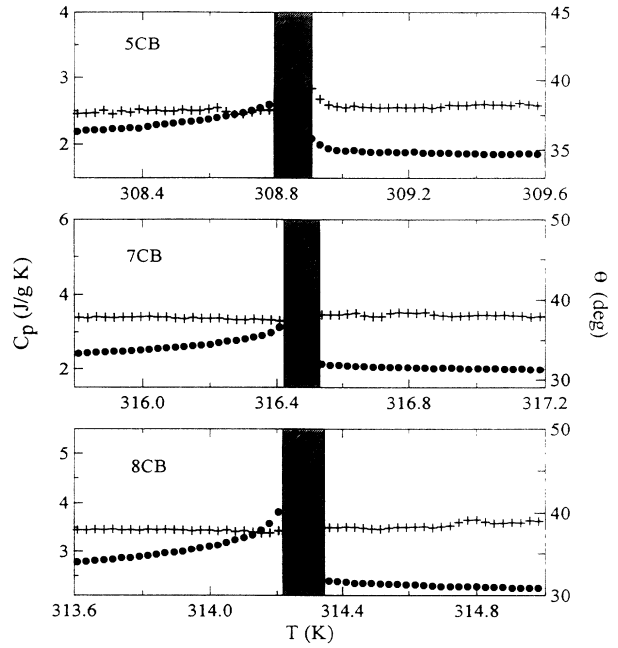

FIG. 11. Typical phase shift (+) and specific heat (●) against temperature near the *N-I* transition for bulk 5CB, 7CB, and 8CB on an expanded scale showing the coexistence region (shaded).

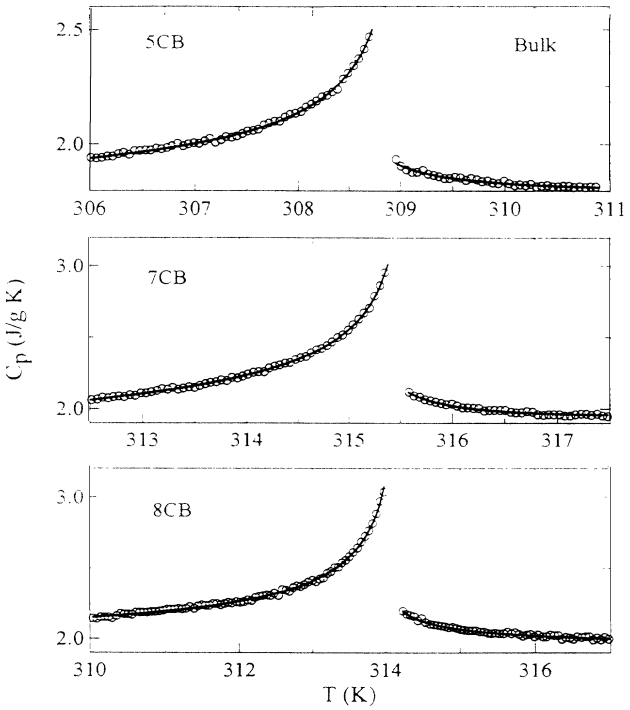

FIG. 12. Specific heat fits (solid lines) to the *N-I* transition using Eq. (9) for *bulk* 5CB, 7CB, and 8CB after removal of the two phase coexistence region. For clarity only every other data point is plotted.

ical behavior [29], an $\alpha=0.5$ is expected.

Equation (9) holds only near T_C, so in actual fits, a region of ± 3 K about T_C is used. Due to its first-order nature, a two-phase coexistence region not related to this critical divergence exists and must be removed, limiting how close to the transition the fit may extend. This coexistence region can be identified as a sudden change in the heat capacity increase (a "kink") or through the phase shift. Figure 11 shows the two-phase region for bulk 5CB, 7CB, and 8CB. For all bulk liquid crystals this region is 0.2 ± 0.05 K wide, compared to 0.16 K wide in high resolution adiabatic calorimetry studies [30]. Thus bulk fits are limited to a reduced temperature range of $10^{-2} \geq |t| > 10^{-4}$.

Fits to the bulk *N-I* transition for 5CB, 7CB, and 8CB are shown in Fig. 12; the fitted parameters are listed in Table II. Combining results from all bulk fits, an average exponent $\alpha=0.51\pm0.04$ is found and is viewed as supporting evidence that the weakly first-order *N-I* transition belongs to the mean field universality class. The ratio of amplitudes $A_-/A_+=3.15\pm0.3$ is much lower than that found for the tricritical behavior of ^{3}He-^{4}He mixtures having $A_-/A_+\cong 8$ [31], suggesting that the *N-I* transition possesses only quasitricritical behavior [28].

For the axial case, the size of the coexistence region increased with increasing carbon chain length of the liquid crystal. Although we lack an explanation, these may be related to the increase in the bulk latent heat (l_{NI}(5CB)=1.56 J/g and I_{nI}(7CB)=2.08 J/g [30]) with

TABLE II. Results of fits using Eq. (9) for the specific heat of bulk 5CB, 7CB, and 8CB at the *N-I* transition. Quoted errors are the statistical uncertainties of the fit parameters. The χ^2 values are the accumulated squared deviations, while $t_{\min}$ is the minimum reduced temperature, calculated by $(T/T_\pm)-1$ [the sign indicating above (+) or below (−) T_{NI}] and for all fits $|t_{\max}|=10^{-2}$.

Bulk	B (J/g K)	D (J/g K)	A_- (J/g K)	A_+ (J/g K)	A/A_+	T_- (K)	T_+ (K)	α	$t_{\min}$	χ^2
5CB	1.72±0.02	2.13±0.5	0.021±0.0006	0.0006±0.002	3.5±0.01	309.06±0.03	308.52±0.04	0.53±0.04	$+1.3\times10^{-3}$ -6.8×10^{-4}	5×10^{-3}
7CB	1.75±0.02	7.58±0.5	0.046±0.008	0.016±0.004	2.88±0.015	315.62±0.02	315.2±0.03	0.46±0.03	$+1.2\times10^{-3}$ -7.6×10^{-4}	8×10^{-3}
8CB	1.89±0.01	0.61±0.3	0.027±0.004	0.009±0.002	3±0.01	314.25±0.01	313.84±0.03	0.53±0.02	$+1.2\times10^{-3}$ -7.7×10^{-4}	2×10^{-3}
Average					3.15±0.3			0.51±0.05		

TABLE III. Results of fits using Eq. (9) for the specific heat of axial 5CB and 7CB at the *N-I* transition. The reported errors are the statistical uncertainties of the fit parameters. The χ^2 values are the accumulated squared deviations.

Axial	B (J/g K)	D (J/g K)	A_- (J/g K)	A_+ (J/g K)	A_-/A_+	T_- (K)	T_+ (K)	α	$t_{\min}$	χ^2
5CB	1.7±0.006	1.94±0.1	0.041±0.003	0.014±0.001	2.93±0.01	308.03±0.004	307.56±0.03	0.42±0.01	$+1.7\times10^{-3}$ -5.0×10^{-4}	6×10^{-3}
7CB	1.74±0.04	3.94±0.8	0.024±0.007	0.009±0.004	2.67±0.03	314.66±0.03	314.22±0.1	0.57±0.05	$+2.1\times10^{-3}$ -8.1×10^{-4}	2×10^{-2}
average					2.80±0.05			0.50±0.07		

the carbon chain length and how it is affected by confinement. The width of data removed from fits to Eq. (9) is 0.22 and 0.49 K for 5CB and 7CB, respectively. Results of axial case fits are summarized in Table III and shown in Fig. 13, yielding an average $\alpha=0.50\pm0.07$ and $A_-/A_+=2.80\pm0.05$. The axially confined *N-I* transition exhibits the same criticality as the bulk case, suggesting that the effect of the axial confinement is to renormalize the temperature scales while merely introducing additional fluctuations that broaden the transition. This is further supported by the enthalpy calculations ΔH, which for the axial cases are within experimental uncertainty the same as the bulk cases. When the axially confined 8CB was fitted according to Eq. (9), it resulted in $T_- < T_+$, a nonphysical result which is a consequence of the large rounded region 0.89 K excluded from the fits.

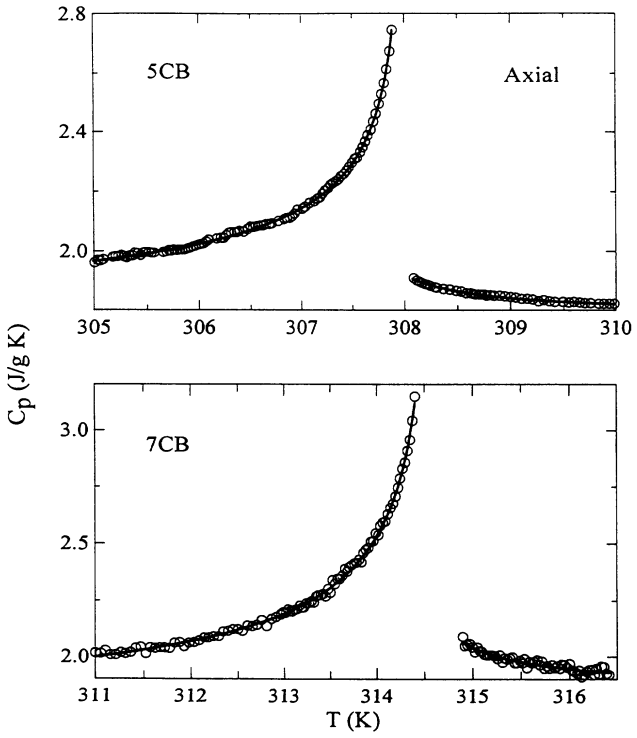

FIG. 13. Specific heat fits (solid lines) to the *N-I* transition using Eq. (9) for *axial* 5CB and 7CB after removal of the two phase coexistence region. For clarity only every other data point is plotted.

Since the radial alignment would require a comparable two-phase region removal, fits were not attempted.

B. The scalar nematic order parameter

The specific heat results at the *N-I* transition reflect the important role played by elastic deformation in confined liquid crystal systems. Elastic deformations can be treated theoretically within the framework of the Landau–de Gennes theory. Such an approach has been successful in interpreting ^{2}H NMR results in confined systems [9]; however, to predict the specific heat behavior requires precise knowledge of the temperature dependence of the free energy (the elastic terms included have temperature dependent coefficients), which is not readily available. Such knowledge does not appear to be required to extract information about an average scalar nematic order parameter Q, starting from the specific heat.

Neglecting details such as biaxiality, a general expression for the approximate heat capacity can be derived from a free energy expansion F in a single scalar order parameter Q. Using the minimization condition $\partial F/\partial Q=0$ and $(\partial/\partial T)[\partial F/\partial Q]=0$ [32], the heat capacity is given by

$$C_p=-T\sum_{i=1}^{n}\left[\left[\frac{\partial^2 F}{\partial T\partial a_i}\right]\left[\frac{\partial a_i}{\partial T}\right]+\left[\frac{\partial F}{\partial a_i}\right]\left[\frac{\partial^2 a_i}{\partial T^2}\right]\right], \tag{10}$$

where the free energy temperature dependence is $F(T)=F(Q(T),a_1(T),a_2(T),\ldots)$ and a_1, a_2, etc. are the coefficients of the expansion. Using a Landau–de Gennes free energy density expansion in terms of the order parameter at the *N-I* transition, $f=f_0+\frac{1}{2}AQ^2+\Theta(Q)$, where $F=fV$, V is the volume, $A=a(T-T^*)$, and $\Theta(Q)$ depend on Q with temperature independent coefficients, leads to

$$\Delta C_p=\frac{1}{2}aVT\left|\frac{\partial(Q^2)}{\partial T}\right| \tag{11}$$

between the heat capacity and the scalar order parameter [29]. This expression is valid when the leading order term in the expansion $\frac{1}{2}AQ^2$ contains the only temperature dependent coefficient. Equation (11) may be extended to free energy models containing nematic spatial fluc-

tuations, surface ordering and disordering terms, and elastic deformations, provided they are included with constant temperature independent coefficients. In general, terms in the free energy expansion which are functions of the order parameter and whose coefficients are temperature independent contribute implicitly to the heat capacity by altering the average order parameter's temperature profile.

From Eq. (11) one finds

$$d(Q^2)=\left[\frac{2}{aV}\right]\frac{\Delta C_p}{T}dT\ , \tag{12}$$

which after integration yields

$$Q_2^2-Q_1^2=\frac{2}{aV}\int_{T_1}^{T_2}\frac{\Delta C_p}{T}dT \tag{13}$$

and the integration limits are obtained as follows. Defining $Q_1=0$ at T_1 sets this temperature well above the *N-I* transition (isotropic phase). The integration of the heat capacity data, after first subtracting a background to find ΔC_p, must be done on cooling $T_1>T_2=T$ and Eq. (13) becomes

$$Q^2(T)=\frac{2}{aV}\int_{T_1}^{T}\frac{\Delta C_p}{T}dT\ . \tag{14}$$

Given the first-order nature, there is a discontinuous jump in the order parameter and a release of latent heat. Since heat capacity measurements by an ac technique are not particularly sensitive to this latent heat, they do not contain direct information about the jump in the order parameter. Such a jump ΔQ_{NI} may be included *ad hoc* by using the entropy $S=-\frac{1}{2}aVQ^2$ [29] and the definition of the latent heat. These are combined to give

$$S_N-S_I=\frac{I_{NI}}{T_{NI}}=\frac{aV}{2}|Q_N^2-Q_I^2|\ , \tag{15}$$

where the subscripts denote the phase (nematic or isotropic) just below and above the transition. Equation (15) yields the jump in Q^2 [$\Delta(Q^2)=Q_N^2-Q_I^2$], which can be converted to the jump in Q [$\Delta Q_{NI}=Q_N-Q_I$] if Q_I is obtained by taking the square root of Eq. (14) at T slightly above T_{NI}. Once ΔQ_{NI} is known, it is added to Eq. (14) for $T<T_{NI}$, in effect shifting upward the baseline of the integration. This determines the scalar order parameter Q_C from thermodynamic quantities alone. The reverse procedure was used in Vycor, which was modeled as composed of independent pore segments [9]. Anopore is naturally a geometry of independent, nonintersecting, cylindrical pores.

Figure 14 shows the model predicted scalar order parameter as a function of reduced temperature, as calculated from the specific heat results for bulk, axial, and radial 5CB of Fig. 6. For the bulk case, the calculated order parameter Q_C exhibits many of the features of the ^{2}H NMR measured Q [10]. On the nematic side of the transition closest to T_{NI}, the magnitude of Q_C starts at 0.31 and increases to ≈ 0.6 well below T_{NI}, in good agreement with experiment. The temperature profiles match reasonably well, only deviating from each other at temperatures much lower than those shown in Fig. 14. In the isotropic phase, Q_C starts at a small value and then decreases to zero with increasing temperature even for the bulk case. This may be a consequence of the derivation of Q_C from a square mean-square root $\sqrt{\langle Q^2\rangle}$, which does not allow nematic/isotropic fluctuations to average to zero.

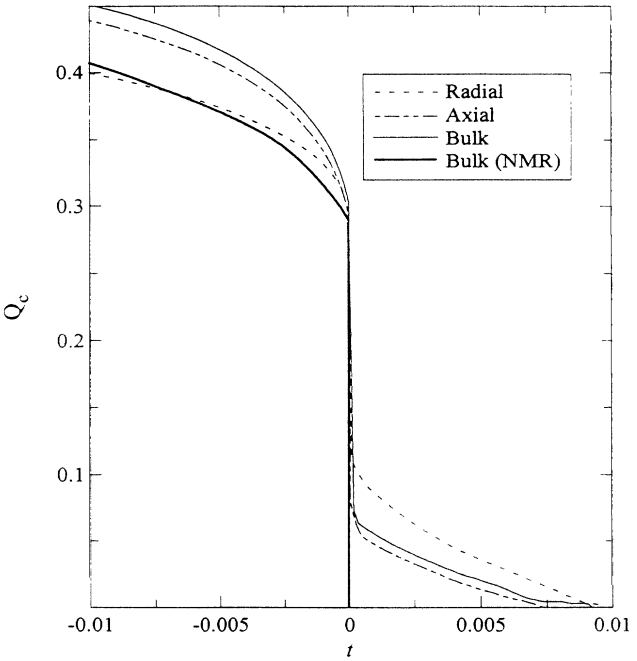

FIG. 14. The model calculated scalar order parameter Q_C for 5CB as a function of reduced temperature for bulk, axial, and radial cases. Also shown is the order parameter for bulk 5CB extrapolated from the NMR results of Ref. [10]. The first-order nature of the Q_C temperature profile is included through the inclusion of the latent heat.

To perform identical calculations for the confined systems requires knowledge of the latent heat of transition, which for simplicity is taken to be that of the bulk case. When plotted as a function of reduced temperature, Fig. 14, the axial behavior Q_C mimics the bulk behavior, but with a slightly smaller value at all temperatures, again illustrating that the axial confinement weakly affects the overall nature of the *N-I* transition. Clearer deviations are seen for the radial confinement; the model predicted order parameter is lower than that of the bulk and the axial case everywhere below T_C, while it is the largest at all temperatures above T_C. This behavior is consistent with NMR results [6], which found residual orientational order for $T>T_C$ and a nematic phase ordered to a lesser degree than that of the bulk case.

C. The smectic-*A* to nematic transition

The characteristics of the Sm-*A*–*N* transition for these systems are summarized in Table IV and shown in Fig. 15. Much stronger effects than those at the *N-I* transi-

TABLE IV. Thermodynamic characteristics of the Sm-$A-N$ transition for bulk, axial, and radial 8CB. ΔT is the T_{AN} shift from bulk, ΔC_p the specific heat amplitude, and ΔH the enthalpy over the same temperature range about the transition. T_{AN}/T_{NI} is the McMillan ratio.

8CB Sm-$A-N$	T_{AN} (K)	ΔT (K)	T_{AN}/T_{NI}	ΔC_p (J/g K)	FWHM (K)	ΔH (J/g)
bulk	307.02		0.978	1.28	0.09	0.48
axial	306.12	−0.9	0.977	0.25	0.79	0.36
radial	306.38	−0.64	0.98	0.11	1.28	0.16

tion are evident. The specific heat peak is greatly suppressed, nearly disappearing for the radial case. The peak maximum for the axial case is 16% that of the bulk case, while for the radial configuration it is only 7.5%. These suppressions are 3.5 and 5 times larger than the corresponding ones at T_{NI}. Over the same temperature range enclosing the transition, the enthalpy ΔH decreases by 25% for the axial case and by 67% for the radial case as compared to the bulk case ($\Delta H_{AN}=0.48 J/g$ while $l_{AN}=0.0014 J/g$ [30]).

Given the larger specific heat suppression and decrease in the enthalpy, an even smaller fraction of the material is undergoing the Sm-$A-N$ transition than the N-I transition. In the axial case and despite its larger specific heat peak, the transition temperature is lower than in the radial alignment. This further eliminates any impurity effects as it is believed that due to the surface treatment, the radial configuration would be more susceptible. In contrast to the bulk case, the nematic range ($T_{NI}-T_{AN}$) is slightly wider in the axial case, but is 1 K narrower in the radial case.

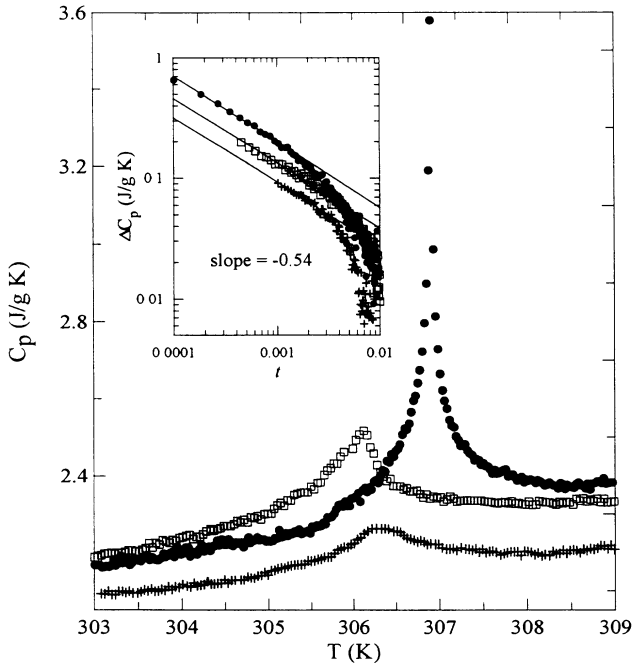

FIG. 15. Specific heat as a function of temperature near the Sm-$A-N$ transition of 8CB for bulk (●), axial (□), and radial (+) configurations. For clarity, the radial data has been shifted down by 0.1 J/g K. Inset: log-log plot of ΔC_p (C_p after background subtraction) vs t illustrating similar critical behavior and the need of the first-order correction-to-scaling term in Eq. (16).

Due to the heterogeneity of the pore surface, we speculate that the axial case may be influenced by weak surface anchoring at diametrically opposed surfaces of the cylindrical pore. Smectic layers that uniformly span the entire diameter of the pore are difficult to form. A shell of nematic material is left near the pore wall that does not participate in the Sm-$A-N$ transition, leading to a smaller peak maximum than in the bulk case. This shell of nematic material, which is completely surrounding the smectic core, acts as a disordering surface for the enclosed smectic phase and lowers T_C.

Radially confined 8CB to the larger pores of lecithin treated glass capillary arrays (25 μm in diameter) was studied by x rays which found distorted smectic layers of variable thickness that formed only near the pore wall [33]. These effects should be more pronounced for the lecithin treated Anopore due its 100 times smaller pore size. Consequently, a thin cylindrical shell of liquid crystal material comprising only a few smectic layers undergoes the Sm-$A-N$ transition, leaving a nematic core in a nearly escaped radial configuration. The smectic region is bordered on one side by a strong orientationally ordering interface (the pore surface); the transition would not be shifted as much as for the axial case. Since fewer smectic layers are formed in the radial case, the specific heat peak maximum would be even smaller. Regardless of configuration, the smectic order is obviously short ranged and the smectic correlating length does not grow beyond a small fraction of the pore size; a translationally disordering nematic phase is preferred within these pores.

Finite size effects should play a role at the Sm-$A-N$ transition. Here there is a distinct difference between the correlation length parallel ($\|$) and perpendicular ($\perp$) to the smectic layers. For 8CB [34] $\xi_\perp \approx |t|^{-\nu(\perp)}$ and $\xi_\| \approx |t|^{-\nu(\|)}$, where $\nu_\perp=0.51$ and $\nu_\|=0.67$. Due to its larger exponent, the parallel component dominates with decreasing system size. To illustrate this, the perpendicular correlation length is comparable to the pore size (1000 Å) only within 0.05 K of the transition, while the parallel correlation length is comparable to it at twice this ΔT. For bulk 8 CB at 0.11 K from T_c (a reduced temperature of 3.5×10^{-4}), $\xi_\| \cong 900$ Å and $\xi_\perp \cong 126$ Å. For the axial confinement, $\xi_\|$ must be compared to the pore radius, while for the radial configuration, $\xi_\|$ must be compared

TABLE V. Fit results of Eq. (16) to the excess specific heat of bulk, axial, and radial 8CB at the Sm-$A-N$ transition. The angular brackets indicate values that were fixed in the final fit and the reported errors are the statistical uncertainties. The χ^2 values are the accumulated squared deviations.

8CB Sm-$A-N$	B_C (J/g K)	A_- (J/g K)	A_+ (J/g K)	A_-/A_+	E_-	E_+	α	T_c (K)	$\lvert t_{\min}\rvert$	χ^2
bulk	-0.55 ± 0.06	0.11 ± 0.02	0.1 ± 0.02	1.08 ± 0.07	4.8 ± 0.3	6.3 ± 0.3	0.26 ± 0.01	307.014 ± 0.0002	5×10^{-5}	2×10^{-2}
axial	-0.05 ± 0.06	0.07 ± 0.02	0.05 ± 0.02	1.37 ± 0.3	-7.4 ± 3	-5.5 ± 4	0.21 ± 0.03	$\langle 306.100\rangle$ fixed	4×10^{-4}	8×10^{-3}
radial	$\langle 0\rangle$ fixed	0.03 ± 0.02	0.03 ± 0.02	0.9 ± 0.6	-11.2 ± 4	-10.3 ± 5	0.21 ± 0.05	$\langle 306.277\rangle$ fixed	1×10^{-3}	4×10^{-3}

to the 60 μm pore length. Thus finite size effects may only play a role in the axial case and only then very close to the transition. The Sm-$A-N$ specific heat suppression is too large to be completely understood in terms of finite size effects.

Critical behavior fits were attempted for the Sm-$A-N$ transition of 8CB to determine the power-law exponent α and the amplitudes ratio. Since the Sm-$A-N$ transition is continuous, the nonphysical situation that arose in the axial N-I case does not occur here; critical fits were attempted for both configurations. For bulk and confined cases, a linear background [$C_b=0.11(\text{J/g K}^2)T$] is subtracted from all data prior to any fitting. The critical part of the specific heat is then fitted using [35]

$$\Delta C_p = B_C + A_\pm |t|^{-\alpha}(1+E_\pm |t|^{0.5}) , \tag{16}$$

where B_C is a small residual background, and the term in parentheses represents a correction-to-scaling term. The Sm-$A-N$ transition belongs to the 3D XY universality class described by a preasymptotic form [36], as supported by recent experiments [37]. This theory predicts $\alpha=-0.007$, $A_-/A_+=0.971$, and $E_-/E_+\cong 1$. However, the Sm-$A-N$ transition is influenced by the proximity of the N-I transition and the preasymptotic 3D XY model is only applicable to systems where the nematic order has completely saturated (a nematic range ≥ 45 K), which is not realized for 8CB (a 7 K nematic range). Then α will be nonuniversal with values for 8CB ranging from 0.25 to 0.33, T_C from 306.60 to 307.02 K, and A_-/A_+ from 0.83 to 1.08 [28,38,39].

Results of fits to the bulk, axial, and radial cases of 8CB are listed in Table V. Fits ranged from

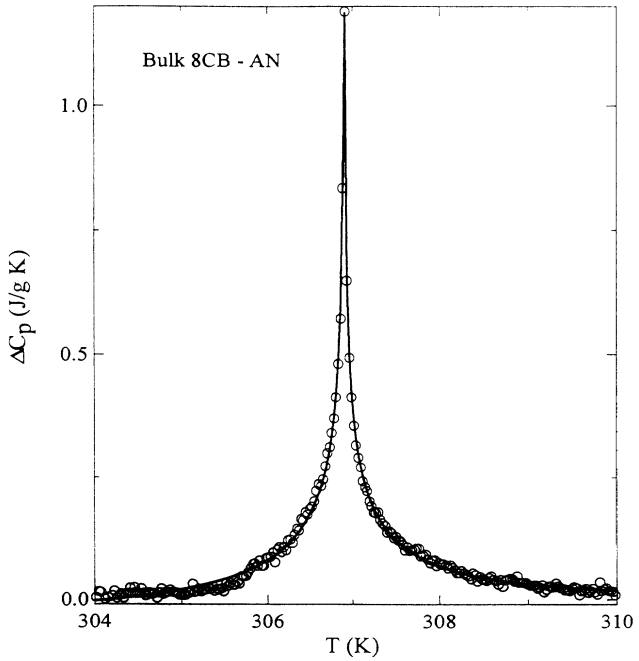

FIG. 16. Excess specific heat fit (solid line) using Eq. (16) for the Sm-$A-N$ transition of *bulk* 8CB. For clarity only every other data point is plotted.

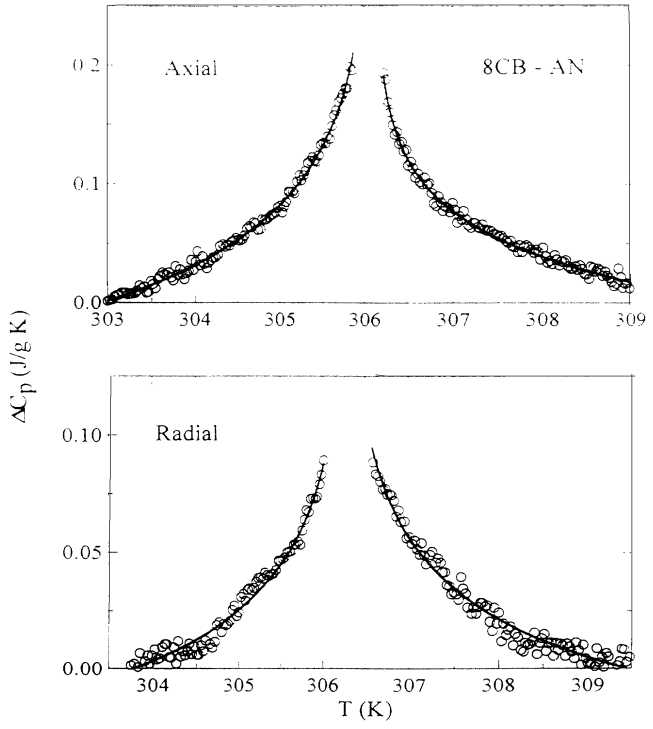

FIG. 17. Excess specific heat fit (solid lines) using Eq. (16) for the Sm-$A-N$ transition of the *axial* and *radial* 8CB configurations. For clarity only every other data point is plotted.

$10^{-2} \geq |t| > 10^{-5}$ for bulk and $10^{-2} \geq |t| > 10^{-3}$ for the confined cases after exclusion of the rounded portions of the peaks. The fit to the bulk Sm-A-N transition of 8CB presented in Fig. 16 was obtained with $\alpha = 0.26 \pm 0.01$, $T_C = 307.014$ K, and $A_-/A_+ = 1.08 \pm 0.07$, values that agree very well with known results [39]. The best fit to the axial case, shown in Fig. 17 with $T_C = 306.10$ K, finds values of α (0.21 ± 0.03) and A_-/A_+ (1.37 ± 0.3) similar to those of the bulk case despite the reduced range of the fit. For the radial confinement with $T_C = 306.277$ K (Fig. 17), the values obtained are also close to bulk ($\alpha = 0.21 \pm 0.05$ and $A_-/A_+ = 0.90 \pm 0.6$), although an even larger region was removed, thus increasing the associated uncertainty. Overall, no appreciable deviations from bulk critical behavior are established, suggesting, as for the axially aligned N-I transition, that a bulklike criticality is retained under these confinements.

D. The smectic-A to isotropic transition

Motivated by the observations at the Sm-A-N transition, we also measured the specific heat for bulk, axial, and radial 10CB, which is shown in Fig. 18. The first-order confined Sm-A-I transition is not shifted to lower temperatures and, surprisingly, the specific heat peak is not severely suppressed. The transition region, which is probably a consequence of our experimental cell setup [8], is quite broad, becoming more rounded for the confined cases. The confinement suppresses in the bulk specific heat signature features that have been attributed to interfacial effects and a temperature dependent surface anchoring energy and were also seen for 12CB [40]. No such features were measured in identically performed measurements with $n < 10$ liquid crystals. In the radial case, the transition is broader and has a small upward temperature shift, similar to the behavior at the Sm-A-N transition in the sense that T_C was higher for the radial than the axial alignment, with both of them below the bulk transition. The parameters that are extracted from the data shown in Fig. 18 are summarized in Table VI.

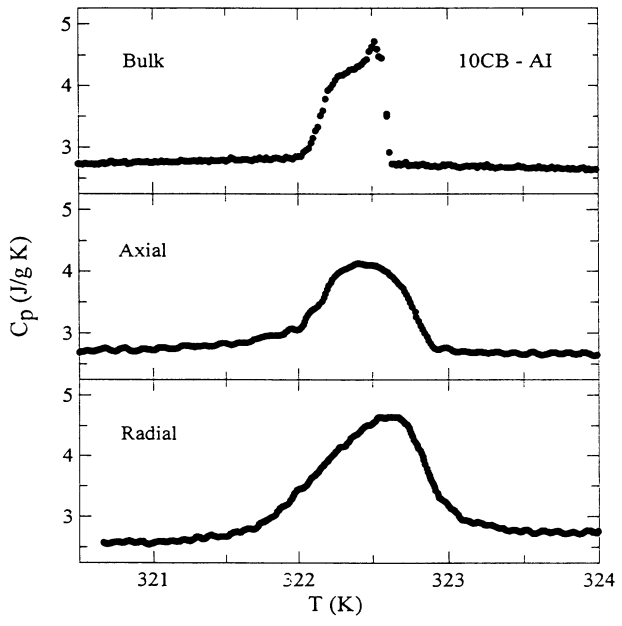

FIG. 18. Specific heat versus temperature near the Sm-A-I transition of bulk, axial, and radial 10CB. Note the insignificant temperature shifts as compared to those at the N-I or Sm-A-N transition.

TABLE VI. Thermodynamic characteristics of the Sm-A-I transition for bulk, axial, and radial 10CB. ΔT is the T_{AI} shift from bulk, ΔC_p the specific heat amplitude, and ΔH the enthalpy over the same temperature range about T_{AI}.

10CB Sm-A-I	T_{AI} (K)	ΔT (K)	ΔC_p (J/g K)	FWHM (K)	ΔH (J/g)
bulk	322.52		2.1	0.43	1.17
axial	322.47	−0.05	1.5	0.71	1.43
radial	322.61	0.09	2.02	0.82	1.99

Despite the particulars, this broad region has large and highly energetic fluctuations, as evident by the calculated enthalpy $\Delta H \approx 1.2$ J/g, which is of the same order of magnitude as that at the N-I (1.2–2 J/g) or Sm-A-N (0.5–0.8 J/g) transitions, but almost completely due to the two-phase coexistence, as we conclude by extrapolating from observations of the bulk phase shift behavior shown in Fig. 2. As a comparison, the latent heat at the 10CB Sm-A-I transition is $l_{AI} = 8.86$ J/K [30]. ΔH increased upon confinement, 1.4 J/g for the axial and 2 J/g for the radial case. This increase in ΔH may be a result of enhanced fluctuations between regions within the pore having a different degree of order. If surface anchoring energies are to play a significant role, as they do for the N-I and Sm-A-N transitions, then they must be comparable in magnitude to the energy of direct smectic fluctuations in an isotropic phase. Taking these results together with those at the Sm-A-N transition, without an intermediate nematic phase in the bulk liquid crystal, a smectic phase is formed within the pores.

IV. CONCLUSIONS

We have described a systematic specific heat study at liquid crystal phase transitions confined to the 0.2 μm diam pores of Anopore membranes, before and after pore surface treatment. This work thoroughly explored confining and orientational effects at the N-I transition and, to a lesser extent, at the Sm-A-N and Sm-A-I transitions of nCB liquid crystals. Bulk results were in agreement with those published in the literature.

At the weakly first-order N-I transition of 5CB, 7CB, and 8CB, the confined specific heat peak for both untreated and lecithin treated Anopore membranes is suppressed, rounded, broad, and shifted to lower temperature as compared to bulk. These effects, although weak for the axial configuration, are nevertheless surprising; they are significantly enhanced for the radial configuration.

The specific heat peak for the axial samples retains a bulklike sharp decrease into the isotropic phase. The two-phase coexistence region for the axial case increases with the liquid crystal carbon chain length. After exclusion of such broad temperature regions, a bulklike criticality appears to be retained under axial confinement.

The radial N-I transition is shifted to even lower temperatures with a greater suppression and broadening of the specific heat peak. For this alignment, the divergent nature of the bulk specific heat is lost and the peak shows a symmetric appearance reminiscent of a continuous transition as also supported by the phase shift signature found, which is more typical of a second-order transition. To be certain, knowledge of possible changes in the thermal diffusion processes or specific heat studies using a technique sensitive to the latent heat of transition is needed. The radial configuration is strongly influenced by elastic distortions and the transition temperature shift is well explained by a simple elastic model. A large two-phase coexistence region prevents an attempt at a critical behavior analysis.

The pore surface is disordering the liquid crystal throughout its diameter, probably due to surface heterogeneity, except for a weakly ordered, thin nematiclike shell pinned by the pore wall. Surface pinning accounts for specific heat suppressions and broadening as it prevents liquid crystal molecules from participating in the transition and enhances the two-phase coexistence between different ordered regions. The surface anchoring energy is an order of magnitude greater for the lecithin treated pore surface than for the untreated pore surface.

A simple empirical method based on a Landau–de Gennes free energy expansion has been described to extract information about the temperature dependence of the average scalar orientational order parameter from the heat capacity data. For the bulk case, the model predictions are in quantitative agreement with NMR measurements, while for the confined systems, its predictions reproduce most of the observed features.

The continuous Sm-A–N phase transition of axial and radial 8CB is significantly more affected than the N-I transition. This is best illustrated in the comparison offered in Fig. 19. The specific heat peak at the Sm-A–N transition is extremely broad and greatly suppressed with a concomitant decrease in the transition enthalpy, which indicates the difficulty of forming smectic layers within these pores whenever a confinement preferred orientationally ordered nematic phase exists in the bulk liquid crystal. This is probably due to the nematic phase providing a mechanism of lowering the free energy of the confined liquid crystal in the presence of elastic distortions and surface disordering. The smectic order is short ranged with the smectic correlation length probably remaining much shorter than the pore size over the temperature range studied. The pore size is too large to attribute these phenomena to finite size effects.

Analysis of the critical behavior at the Sm-A–N transition finds that despite the removal of a large rounded region, the transition for both alignments retains a bulklike criticality. The emerging physical picture consists of smectic order occurring most likely near the pore wall for the radial case, while taking place near the pore center for the axial case. We conjecture that this may be due to the strong surface alignment introduced in the radial case which allows the formation of only a few smectic layers parallel to the pore wall. For the axial case, surface disordering retains a nematic shell near the wall at all temperature, allowing only material far from the pore wall to form a smectic phase parallel to the pore axis.

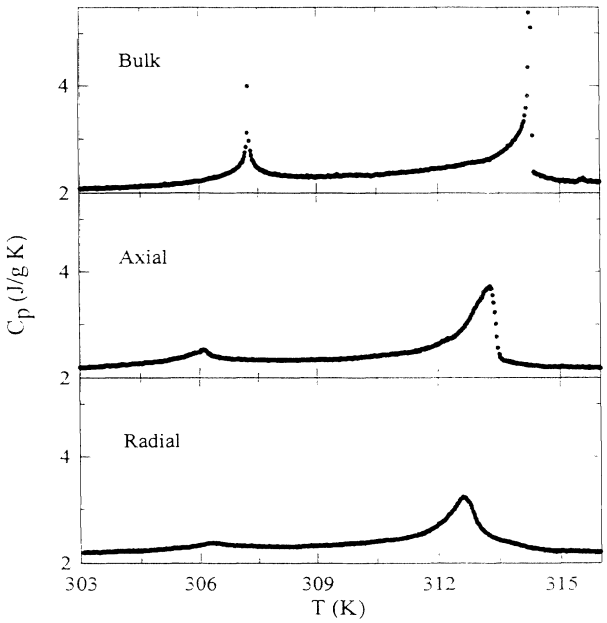

FIG. 19. Comparison of the specific heat over a wide temperature range and using the same specific heat scale to emphasize the differences between the N-I and Sm-A–N transition for bulk, axial, and radial 8CB configurations.

For the unexpectedly broad first-order Sm-A–I transition of 10CB, most of the effects observed at the N-I and Sm-A–N transition are absent. The specific heat peak position hardly shifts in temperature, being slightly higher for the radial alignment. The transition is broader for the axial case and broader still for the radial case, resulting in an increase in the transition enthalpy from the bulk to the axial to the radial case. The absence of a nematic phase in the bulk permits smectic layers to form within the pores, possibly with the exception of a nematiclike shell at the pore wall which is not allowed to grow. To appreciably affect the bulk transition, energies from elastic distortions and surface disordering must be large to compete with the inherently higher free energy of the Sm-A–I transition.

Further experimental efforts should focus on the translational order in such confined systems which can be tested through x-ray and light scattering studies. Specific heat studies should be extended by systematically changing the anchoring energy and pore size. The former can be achieved by treating Anopore with a variable aliphatic acid chain, while the latter by employing Nuclepore

membranes. Recent ^{2}H NMR work for 5CB in Anopore treated with variable chain length aliphatic acid found evidence of a director configuration transition as well as a wetting transition [41], which may be related to some of the phenomena observed here. Confined studies should include wider range nematics, nonpolar, and even chiral liquid crystals. Effects on the tricritical behavior for liquid crystal mixtures and the melting transition, which will likely show large supercooling effects, are yet to be explored. Theoretical efforts addressing the behavior of liquid crystals in porous media are needed.

ACKNOWLEDGMENTS

We have benefitted from multiple discussions with David Allender, Greg Crawford, Bill Doane, Carl Greeff, Mike Lee, Renata Marroum, Peter Palffy-Muhoray, and Slobodan Zumer. This work was supported by NSF through the ALCOM-STC Grant No. DMR 89-20147. Liquid crystals were purified and provided by Sandy Keast and Mary Neubert through the ALCOM Resource Facility. One of us (D.F.) thanks the Research Council of Kent State University for its support.

[1] M. P. A. Fisher, P. B. Weichman, G. Grinstein, and D. S. Fisher, Phys. Rev. B **40**, 546 (1989), and references therein.
[2] W. Krauth, N. Trivedi, and D. Ceperley, Phys. Rev. Lett. **67**, 2307 (1991).
[3] C. J. Yeager, L. M. Steele, and D. Finotello, Phys. Rev. B **49**, 9782 (1994).
[4] N. A. Clark, T. Bellini, R. M. Malzbender, B. N. Thomas, A. G. Rappaport, C. D. Muzny, D. W. Schaefer, and L. Hrubesh, Phys. Rev. Lett. **71**, 3505 (1993).
[5] G. P. Crawford, D. K. Yang, S. Zumer, D. Finotello, and J. W. Doane, Phys. Rev. Lett. **66**, 723 (1991).
[6] G. P. Crawford, R. Stannarius, and J. W. Doane, Phys. Rev A **44**, 2558 (1991).
[7] D. W. Allender, G. P. Crawford, and J. W. Doane, Phys. Rev. Lett. **67**, 1442 (1991).
[8] G. S. Iannacchione and D. Finotello, Phys. Rev. Lett. **69**, 2094 (1992).
[9] G. S. Iannacchione, G. P. Crawford, S. Zumer, J. W. Doane, and D. Finotello, Phys. Rev. Lett. **71**, 2595 (1993).
[10] A. Golemme, Ph.D. thesis, Kent State University, 1987.
[11] L. M. Steele, C. J. Yeager, and D. Finotello, Phys. Rev. Lett. **71**, 3673 (1993).
[12] L. M. Steele, G. S. Iannacchione, and D. Finotello, Rev. Mex. Fis. **39**, 588 (1993).
[13] P. Sullivan and G. Seidel, Phys. Rev. **173**, 679 (1969).
[14] D. Finotello, K. A. Gillis, A. Wong, and M. H. W. Chan, Phys. Rev. Lett. **61**, 1954 (1988).
[15] K. Ghiron, M. B. Salamon, B. W. Veal, A. P. Paulikas, and J. W. Downey, Phys. Rev. B **46**, 5837 (1992).
[16] C. W. Garland, in *Phase Transitions in Liquid Crystals*, edited by S. Martellucci and A. N. Chester (Plenum, New York, 1992), p. 175 and references therein.
[17] T. Stoebe, R. Geer, C. C. Huang, and J. W. Goodby, Phys. Rev. Lett. **69**, 2090 (1992).
[18] Anopore available from Whatman Laboratories Div., 9 Bridewell Place, Clifton, NJ 07014.
[19] R. C. Furneaux, W. R. Rigby, and A. P. Davidson, Nature (London) **337**, 147 (1989).
[20] G. P. Crawford, L. M. Steele, G. S. Iannacchione, R. Ondris-Crawford, C. J. Yeager, J. W. Doane, and D. Finotello, J. Chem. Phys. **96**, 7788 (1992).
[21] G. P. Crawford, D. W. Allender, and J. W. Doane, Phys. Rev. A **45**, 8693 (1992).
[22] T. Bellini, N. A. Clark, C. D. Muzny, L. Wu, C. W. Garland, D. W. Schaefer, and B. J. Oliver, Phys. Rev. Lett. **69**, 788 (1992).
[23] M. Kuzma and M. M. Labes, Mol. Cryst. Liq. Cryst. **100**, 103 (1983).
[24] M. A. Anisimov, Mol. Cryst. Liq. Cryst. A **162**, 1 (1988).
[25] F. M. Aliev and M. N. Breganov, Zh. Eksp. Teor. Fiz. **95**, 122 (1989) [Sov. Phys. JETP **68**, 70 (1989)].
[26] L. M. Blinov, E. I. Kats, and A. A. Sonin, Usp. Fiz. Nauk **152**, 449 (1987) [Sov. Phys. Usp. **30**, 604 (1987)].
[27] A. R. Ubbelohbe, *Melting and Crystal Structure* (Clarendon, Oxford, 1965).
[28] G. B. Kasting, C. W. Garland, and K. J. Lushington, J. Phys. **41**, 879 (1980); G. B. Kasting, K. J. Lushington, and C. W. Garland, Phys. Rev. B **22**, 321 (1980).
[29] M. A. Anisimov, V. Mammitskii, and E. Sorkin, J. Eng. Phys. (USSR) **39**, 1385 (1981); M. A. Anisimov, *Critical Phenomena in Liquids and Liquid Crystals* (Gordon and Breach, New York, 1991); M. A. Anisimov, V. M. Zaprudskii, V. M. Mamnitskii, and E. L. Sorkin, Pis'ma Zh. Eksp. Teor. Fiz. **30**, 523 (1979) [JETP Lett. **30**, 491 (1979)]; M. A. Anisimov, E. E. Gorodetskii, and V. M. Zaprudskii, Usp. Fiz. Nauk **133**, 103 (1981) [Sov. Phys. Usp. **24**, 57 (1981)].
[30] J. Thoen, in *Phase Transitions in Liquid Crystals* (Ref. [16]), p. 155.
[31] S. T. Islander and W. Zimmermann, Jr., Phys. Rev. A **7**, 188 (1973).
[32] This is a consequence of $Q(T)$ minimizing $F(T)$ at every temperature.
[33] J. T. Mang, K. Sakamoto, and S. Kumar, Mol. Cryst. Liq. Cryst. **223**, 133 (1992).
[34] J. D. Litster, J. Als-Nelson, R. J. Birgeneau, S. S. Dana, D. Davidov, F. Garcia-Golding, M. Kaplan, C. R. Safinya, and R. Schaetzing, J. Phys. C **3**, 339 (1979).
[35] P. Das, G. Nounesis, C. W. Garland, G. Sigaud, and N. H. Tinh, Liq. Cryst. 7, 883 (1990).
[36] B. R. Patton and B. S. Andereck, Phys. Rev. Lett. **69**, 1556 (1992).
[37] G. Nounesis, K. I. Blum, M. J. Young, C. W. Garland, and R. J. Birgeneau, Phys. Rev. E **47**, 1910 (1993); C. W. Garland, G. Nounesis, M. J. Young, and R. J. Birgeneau, *ibid.* **47**, 1918 (1993).
[38] I. Hatta and T. Nakayama, Mol. Cryst. Liq. Cryst. **66**, 97 (1981).
[39] J. Thoen, H. Marynissen, and W. van Dael, Phys. Rev. A **26**, 2886 (1982).
[40] G. Iannacchione, A. Strigazzi, and D. Finotelli, Liq. Cryst. **14**, 1153 (1993).
[41] G. Crawford, R. Ondris-Crawford, S. Zumer, and J. Doane, Phys. Rev. Lett. **70**, 1838 (1993).

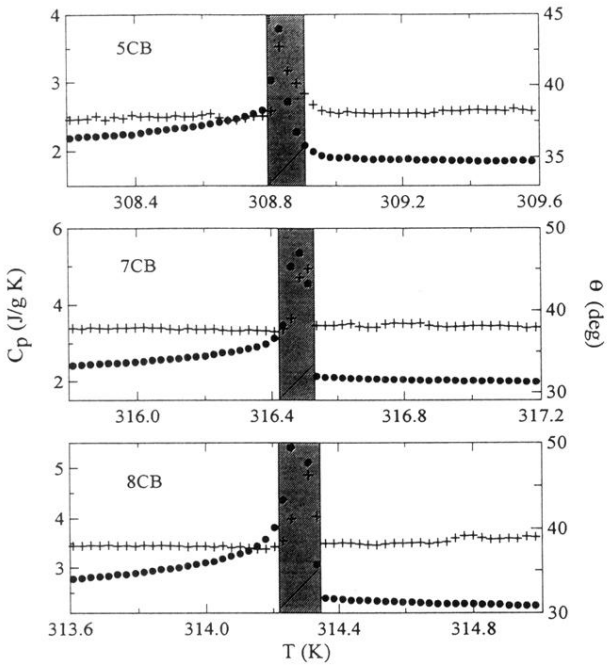

FIG. 11. Typical phase shift (+) and specific heat (●) against temperature near the *N-I* transition for bulk 5CB, 7CB, and 8CB on an expanded scale showing the coexistence region (shaded).

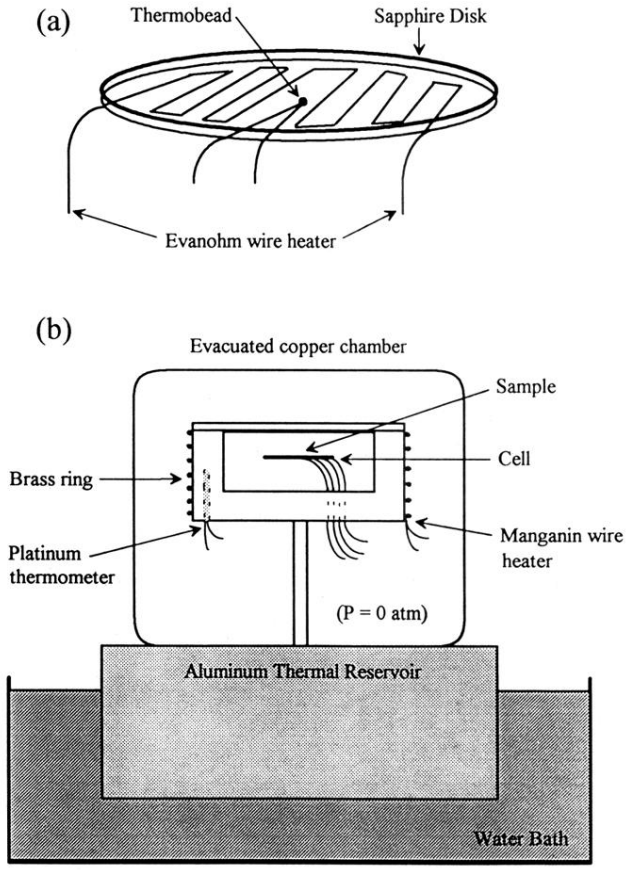

FIG. 4. Illustration of (a) the calorimeter cell and (b) the experimental support apparatus.

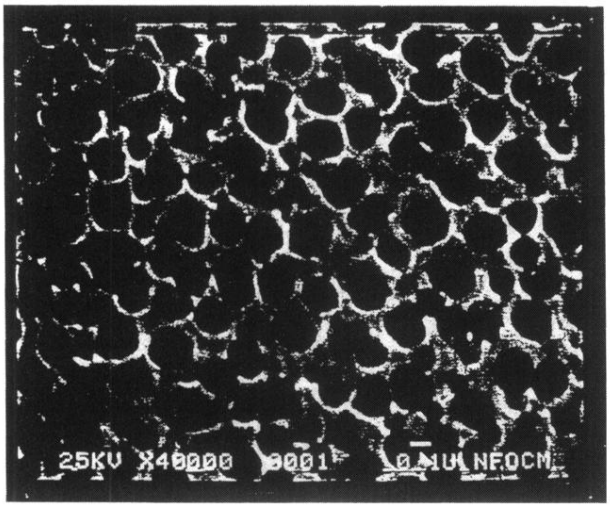

FIG. 5. SEM photograph of the 0.2 μm diam pores of Anopore membrane.